Citation (APA)
Brudanin, V., Rieger, B., & Stallinga, S. (2026). Generalized low-pass filtering in structured illumination microscopy and spatial domain reconstructions with high signal-to-noise ratio. *Optics Express*, *34*(12), 22940-22963.
https://doi.org/10.1364/OE.603209

Research Article | Vol. 34, No. 12 / 15 Jun 2026 / Optics Express 22940

Optics EXPRESS

Generalized low-pass filtering in structured illumination microscopy and spatial domain reconstructions with high signal-to-noise ratio

VALERII BRUDANIN, BERND RIEGER, AND SJOERD STALLINGA*

Department of Imaging Physics, Delft University of Technology, The Netherlands
*s.stallinga@tudelft.nl

Abstract: Structured illumination microscopy (SIM) is a technique that employs non-uniform illumination to shift spatial frequencies that are normally unobservable into the non-zero region of the optical transfer function (OTF). Several differently illuminated images are combined to reconstruct these high spatial frequencies, yielding an up to two-fold increase in resolution beyond the diffraction limit. The reconstruction quality is affected by the noise level which depends on the specific procedure. In this work, we show that least-squares Fourier domain reconstruction results in the best possible theoretically achievable SSNR and thus can serve as a metric for reconstruction quality. We consider, in a general manner, how the choice of low-pass filtering in the reconstruction procedure affects the spectral signal-to-noise ratio (SSNR) in the reconstructed image. Finally, we present fast real-space reconstruction procedures that demonstrate near-optimal noise performance.

1. Introduction

In the context of fluorescent microscopy, Structured Illumination Microscopy (SIM) [1–3] belongs to a broad family of super-resolution methods, which expand the region of spatial frequencies that can be transferred by an optical system, by exploiting non-uniform illumination of the fluorescent sample. This family can be, at least in practice, divided into methods that provide optical sectioning without going beyond the diffraction limit (confocal microscopy (CM) [4], light sheet microscopy (LSM)) and those that achieve super-resolution (image scanning microscopy (ISM) [5,6] and the closely related re-scan technique [7], stimulated emission depletion (STED) [8,9] and SIM). In all cases, super-resolution is achieved by adding prior knowledge about the illumination pattern incident on the sample. However, several observations are always required to achieve super-resolution. In point-scanning techniques, observations are often single values that correspond to the total light energy collected for different illumination focus point positions. The reconstructed image is then just a collection of these observations for each scan position of the point-like illumination pattern (CM, STED). ISM presents an example of a point-scanning method with a more complicated reconstruction procedure [6,10], improvements of which have been found to this day [11,12]. The necessity of scanning the sample significantly limits the acquisition speed of point-scanning methods, making them unsuitable for imaging of rapid cellular processes. In SIM, on the other hand, the sample is illuminated with a spatially periodic pattern across the whole field of view (FOV). Typically, modulation is achieved as a result of interference of several electromagnetic plane waves in one or several directions [3,13,14]. The resulting pattern of sinusoidal type is phase-shifted several times to obtain distinct illuminations. This choice allows for an out-of-band reconstruction by solving a system of linear equations [2,3] and theoretical estimation of the signal-to-noise ratio [15,16].

#603209
Journal © 2026
https://doi.org/10.1364/OE.603209
Received 20 Apr 2026; revised 26 May 2026; accepted 26 May 2026; published 11 Jun 2026

Optics EXPRESS

There are different ways to approach the SIM reconstruction problem. Due to the imminent presence of noise, the system of equations to solve is stochastic. Thus, one must first define the loss function that is minimized by the solution. Moreover, because of the band-limited nature of the optical system, the inversion of the SIM system of equations is ill-defined. Regularization is required at high spatial frequencies to prevent noise amplification. The task of choosing a regularization filter for SIM reconstructions was considered in detail in Ref. [16]. Another challenge imposed by the finite support of the Optical Transfer Function (OTF) is apodization of the reconstructed object. To match physical intuition, a final super-resolution image should satisfy the criteria of non-negativity and high contrast [17]. Possible options for apodization in SIM were studied in [17,18].

Broadly speaking, there are two types of SIM reconstruction approaches: Fourier domain reconstruction (FDR) and spatial domain reconstruction (SDR). Although the spatial and Fourier domain present mathematically equivalent but alternative routes to work with the same information, their practical implementation differs. Fourier domain reconstruction seems the natural approach due to the possibility of contrast enhancement by standard filtering in Fourier space. A commonly used Fourier domain reconstruction procedure that optimizes the least-squares (LS) loss function, ensures a high spectral signal-to-noise ratio [15,16]. However, FDR requires multiple Fourier transformations, which become a computational burden for large 3D image datasets. Another disadvantage of FDR is the intrinsic assumption that experimental quantities, such as the point spread function (PSF), the refraction index, and the modulation depth of the pattern, remain constant across the whole FOV. For large FOV and deep tissue imaging, these assumptions are violated. Field-dependent aberrations distort the PSF across the FOV [19], and the apparent modulation coefficients decrease due to light scattering. If SIM is combined with another technique, for example, selective-plane illumination [20] or selective-plane activation [21], additional aberrations will be introduced due to light-sheet non-uniformity. These factors introduce unknown effects into the image reconstruction.

The spatial domain reconstructions [22–26] that were proposed for conventional [23,25] and lattice [26] SIM are performed completely in real space, and a 7-fold computational acceleration was reported due to the absence of Fourier transforms [23]. In addition, in [22,23,26] the reconstructed image is obtained by inversion of the illumination pattern, making the reconstruction procedure completely local. However, in this way, no merit function is optimized, and hence no robustness of the reconstruction towards noise is guaranteed.

In [16] it was noticed that the Spectral Signal-to-Noise Ratio (SSNR) of the reconstructed image depends only on a certain part of the full reconstruction procedure. Fourier filtering for regularization and apodization affect the contrast and visual appearance of the image, but not the SSNR. In other words, filtering can make the image appear more similar to the ground truth, but the level of statistical correlation between the two is not affected. The famous Shannon channel capacity theorem [27] states that the SNR and the amount of information transferred through the channel are directly related quantities. Inspired by the theory of information transfer [28], we can consider microscopy image modalities like SIM to consist of an encoding stage, in which information about the object is encoded in the sample during the acquisition, and a decoding stage, in which the acquired images are combined into a super-resolution image during the reconstruction. The effect of experimental parameters (illumination configuration, pitch of the illumination pattern, illumination phase shifts) on SNR in SIM has been studied in multiple works [13–15].

In this work, we investigate the decoding stage of SIM reconstruction in a general way. We start with setting up a general framework for the image reconstruction procedure that contains SDR and FDR methods mentioned above as special cases. We use this framework to derive an expression for the SSNR of these reconstructions and prove that the least-squares FDR results in the best SSNR at each spatial frequency. We then use the optimal least-squares reconstruction

Optics EXPRESS

SSNR as a baseline for comparison to other reconstructions. We show that the overly simplified SDR approach [23,25] saves computational time but leads to an order-of-magnitude reduction in the SSNR at high spatial frequencies. Finally, we explain how we can achieve high SSNR in the spatial domain using convolution with a small kernel directly in real space. We propose appropriate kernels and verify our theory with the reconstructions of simulated and experimental 2D and 3D SIM images.

2. Generalized framework for SIM reconstructions

2.1. Preliminaries

We adopt the continuum image formation model for the sake of analytical simplicity and later perform the transition to a discrete, pixelized case. For the same reason, we first consider the case where the illumination pattern is only shifted but not rotated.

We adopt the following convention for the Fourier transformation and inverse, from real space coordinates $\vec{r}$ to reciprocal coordinates $\vec{q}$:

$$\begin{aligned} \hat{F}(\vec{q}) &= \int d\vec{r}\, e^{-2\pi i \vec{q}\vec{r}} F(\vec{r}) \\ F(\vec{r}) &= \int d\vec{q}\, e^{2\pi i \vec{q}\vec{r}} \hat{F}(\vec{q}) \end{aligned} \tag{1}$$

where we designate the function in reciprocal space with a hat ˆ on top.

The transition to the discrete, pixelized, case can be performed if the Nyquist sampling condition is satisfied. Continuous coordinates $\vec{r}$ and $\vec{q}$ must be replaced with their discrete versions $\vec{r}_j$ and $\vec{q}_j$ and all integrations by summation. The forward and inverse discrete Fourier transforms follow the same sign convention as in (1), and the forward Fourier transformation accommodates an additional numeric prefactor $1/N$ where N is the total number of pixels of the image.

In the process of image acquisition by an optical system with the PSF $g(\vec{r})$, we obtain $n = 1, 2, \ldots, M_t$ images $I^n(\vec{r})$ corresponding to displaced illumination patterns $h^n(\vec{r})$.

$$I^n(\vec{r}) = \int d\vec{r}F'\, g(\vec{r} - \vec{r}')h^n(\vec{r}')f(\vec{r}') \tag{2}$$

where $f(\vec{r})$ is the true unknown fluorophore distribution, and where $h^n(\vec{r}) = h(\vec{r} - \vec{u}_n)$ with $\vec{u}_n$ the displacement vector for the n-th pattern.

Our subsequent derivations are based on several assumptions. First, the illumination excitation intensity pattern $h(\vec{r})$ must be decomposable into a finite sum of plane waves:

$$h(\vec{r}) = \sum_{\underline{m}}^{M} a_{\underline{m}} \exp\left(2\pi i \vec{k}_{\underline{m}} \cdot \vec{r}\right) . \tag{3}$$

We use the notation $a_{\underline{m}}$ for the modulation coefficients (amplitudes) of the expansion plane waves and $\vec{k}_{\underline{m}}$ for the spatial frequency vectors of the plane waves. We assume that there are M spatial plane waves in total. Second, the spatial frequency vectors must span a Bravais lattice in Fourier space labeled by lateral indices $\underline{m} = (m_1, m_2)$:

$$\vec{k}_{\underline{m}} = m_1\vec{b}_1 + m_2\vec{b}_2 \,. \tag{4}$$

where $\vec{b}_1$ and $\vec{b}_2$ are basis vectors of the lattice. Third and finally, we must be able to select a set of illumination pattern translations $\vec{u}_n$, which satisfies a so-called orthogonality condition

$$\sum_{n=1}^{M_t} \exp\left(2\pi i \left(\vec{k}_{\underline{m}} - \vec{k}_{\underline{m}'}\right) \vec{u}_n\right) = M_t \delta_{\underline{m},\underline{m}'} = M_t \delta_{m_1 m_1'} \delta_{m_2 m_2'}, \tag{5}$$

where M_t is the total number of translations.

Optics EXPRESS

There are two reasons why we want conditions (4) and (5) to be satisfied. First, they allow for a straightforward inversion procedure of the phase matrix [16], and we will use (5) to derive an equivalent real-space procedure, similar to those in [23,26]. Second, the orthogonality condition (5) is equivalent to the statement that the phase matrix is unitary [13], which means that its condition number equals 1 in L2. An inappropriate choice of phase shifts may result in a high condition number and therefore lead to numeric instabilities in the reconstruction [29].

These assumptions are quite general. Equation (3) is satisfied automatically if the illumination pattern is formed with a finite number of electromagnetic plane waves which is always the case in any real experiment [14]. Equation (4) restricts the number of possible back focal plane configurations of the electromagnetic plane waves but is satisfied in practice for conventional one-dimensional sinusoidal sample modulation [2] or square [26] and hexagonal [30] lattice patterns. Equation (5) can also be always satisfied in practice as in [13] it was shown that not only one-dimensional modulation patterns but also two-dimensional ones with square and hexagonal symmetry allow a set of one-directional shifts $\vec{u}_n = n\vec{s}$ with the basis vector $\vec{s}$ and $n = 0, 1, \ldots, M_t - 1$ such that the orthogonality condition is satisfied.

2.2. Reconstruction framework

Here, we set up a generalized framework for SIM reconstruction that has FDR and SDR as special cases. The general expression for this SIM reconstruction is the sum over all pattern translations

$$I^{SR}(\vec{r}) = \sum_{n=1}^{M_t} C^n(\vec{r}) I_K^n(\vec{r}), \tag{6}$$

where $C^n(\vec{r})$ are to-be determined position-dependent coefficients, and where

$$I_K^n(\vec{r}) := K(\vec{r}) \otimes I^n(\vec{r}) = \int d\vec{r}'\, G(\vec{r} - \vec{r}') h^n(\vec{r}') f(\vec{r}'), \tag{7}$$

with $G(\vec{r}) = K(\vec{r}) \otimes g(\vec{r})$ and $\otimes$ denotes the convolution operation. In this equation, we convolve the acquired images with a mathematically arbitrary kernel $K(\vec{r})$. The convolution with such a kernel corresponds to the filtering operation in the Fourier domain, and we show later that it is crucial for achieving good SSNR in the final image.

The choices of reconstruction that we have in this framework are therefore the functions $C^n(\vec{r})$ and the convolution kernel $K(\vec{r})$. It appears, however, that the form of the $C^n(\vec{r})$ is limited by the requirement that the overall reconstruction can be described as a linear shift-invariant representation of the object

$$I^{SR}(\vec{r}) = \int d\vec{r}'\, g^{SR}(\vec{r} - \vec{r}') f(\vec{r}'), \tag{8}$$

where g^{SR} is the resulting super-resolution PSF of the SIM reconstruction. Comparing (8) and (6) we see that $g^{SR}(\vec{r} - \vec{r}')$ must be expressed as

$$g^{SR}(\vec{r} - \vec{r}') = \sum_{n=1}^{M_t} C^n(\vec{r}) G(\vec{r} - \vec{r}') h^n(\vec{r}') = G(\vec{r} - \vec{r}') \sum_{n=1}^{M_t} C^n(\vec{r}) h^n(\vec{r}'). \tag{9}$$

It thus appears that (9) can only be satisfied in very specific cases, because the left-hand side depends on the difference of $\vec{r}$ and $\vec{r}'$, while the right-hand side generally depends on $\vec{r}$ and $\vec{r}'$ separately. In other words, this puts a constraint on the possible form of the $C^n(\vec{r})$.

We will now use this constraint to derive an explicit and simple form for the $C^n(\vec{r})$. To that end, we first substitute in Eq. (9) the expansion of the illumination pattern in its harmonic components to give

$$\sum_{n=1}^{M_t} C^n(\vec{r})h^n(\vec{r}') = \sum_{\underline{m}} C^n(\vec{r})a_{\underline{m}}e^{2\pi i\vec{k}_{\underline{m}}\cdot(\vec{r}'-\vec{u}_n)}, \tag{10}$$

and perform a change of variables $\vec{r}' = \vec{r} - \vec{R}$ so that

$$G(\vec{R})\sum_{n=1}^{M_t}\sum_{\underline{m}} a_{\underline{m}}e^{2\pi i\vec{k}_{\underline{m}}\cdot(\vec{r}-\vec{R}-\vec{u}_n)}C^n(\vec{r}) = g^{SR}(\vec{R}). \tag{11}$$

Taking the FT to reciprocal space $\vec{R} \to \vec{Q}$ gives

$$\hat{g}^{SR}(\vec{Q}) = \sum_{\underline{m}} a_{\underline{m}}\hat{G}(\vec{Q}+\vec{k}_{\underline{m}})e^{2\pi i\vec{k}_{\underline{m}}\cdot\vec{r}}\sum_{n=1}^{M_t} e^{-2\pi i\vec{k}_{\underline{m}}\cdot\vec{u}_n}C^n(\vec{r}). \tag{12}$$

This equation should hold for any $\vec{Q}$ and for any $\vec{r}$. This is only possible if

$$\sum_{n=1}^{M_t} e^{-2\pi i\vec{k}_{\underline{m}}\cdot\vec{u}_n}C^n(\vec{r}) = w_{\underline{m}}e^{-2\pi i\vec{k}_{\underline{m}}\cdot\vec{r}}, \tag{13}$$

for some set of constants $w_{\underline{m}}$. If we now invoke assumption (5) about the unitarity of the phase matrix an explicit expression for the $C^n(\vec{r})$ follows as

$$C^n(\vec{r}) = \frac{1}{M_t}\sum_{\underline{m}} w_{\underline{m}}e^{-2\pi i\vec{k}_{\underline{m}}\cdot(\vec{r}-\vec{u}_n)}. \tag{14}$$

We see that the functions $C^n(\vec{r})$ have the same Fourier expansion as the illumination pattern, including the pattern shifts, but now with in principle arbitrary Fourier order coefficients.

Substituting (14) back into (12), we obtain the solution for the super-resolution OTF $\hat{g}^{SR}(\vec{Q})$

$$\hat{g}^{SR}(\vec{Q}) = \sum_{\underline{m}} a_{\underline{m}}w_{\underline{m}}\hat{G}(\vec{Q}+\vec{k}_{\underline{m}}) = \sum_{\underline{m}} a_{\underline{m}}w_{\underline{m}}\hat{K}(\vec{Q}+\vec{k}_{\underline{m}})\hat{g}(\vec{Q}+\vec{k}_{\underline{m}}). \tag{15}$$

We thus arrive at a generalized version of the known result that in the Fourier domain the super-resolution OTF is a sum of scaled shifted and low-passed copies of the real physical OTF [16]. The super-resolution PSF is found after IFT as

$$g^{SR}(\vec{r}) = (K(\vec{r})\otimes g(\vec{r}))\sum_{\underline{m}} a_{\underline{m}}w_{\underline{m}}\exp(-2\pi i\vec{k}_{\underline{m}}\cdot\vec{r}). \tag{16}$$

One can see that a particular SIM reconstruction is defined by the choice of the kernel $K(\vec{r})$ and the modulation coefficients $w_{\underline{m}}$. The case of FDR is found for the choices $K(\vec{r}) = g(\vec{r})$ and $w_{\underline{m}} = a_{\underline{m}}$, i.e. low-pass filtering by convolving with the physical PSF, and taking functions $C^n(\vec{r})$ that are equal (up to an overall constant) to the illumination pattern. The case of SDR is found for the choices $K(\vec{r}) = 1$ and $w_{\underline{m}} = 1$, i.e. no low-pass filtering at all is applied, and equal strength of all harmonic components of the functions $C^n(\vec{r})$. In this case there is the simple-looking expression for the reconstruction procedure

$$I^{SR}(\vec{r}) = \sum_{n=1}^{M_t} h^n(\vec{r})I^n(\vec{r}). \tag{17}$$

If the illumination pattern is rotated $M_r>1$ times and no assumptions (3–5) are violated at any angle, the reconstruction procedures can be performed without changes for each rotation separately. The super-resolution images corresponding to one rotation r are then added with some weights, typically the same, to produce the final image, and

$$g^{SR}(\vec{r}) = (K(\vec{r}) \otimes g(\vec{r})) \sum_{r=1}^{M_r} \sum_{\underline{m}} a_{\underline{m}r} w_{\underline{m}r} \exp(-2\pi i k_{\underline{m}r} \vec{r}) \,. \tag{18}$$

We will mainly omit the rotational index r in our further derivations.

2.3. 3D SIM

Today 3D SIM data acquisition and reconstruction procedures typically follow the approach from [3]. In this approach, the illumination is kept fixed with respect to the focal plane, which is not the same as if it was fixed with respect to the sample [29]. In a standard procedure, the 3D image stack is acquired slice by slice by moving the sample holder, and as a result not all OTF copies are separated [3]. In this case, some modifications to the 2D formalism are needed. The image formation model changes to

$$I^{SR}(\vec{r}) = \int d\vec{r}'\, g(\vec{r} - \vec{r}')h(x', y', z' - z)f(\vec{r}') \,. \tag{19}$$

From [3] we know that SIM reconstruction in the Fouirer domain remains mostly the same as in 2D, but we can no longer consider illumination modulation coefficients and shifted OTF copies separately. We must instead convolve the illumination pattern expansion in the axial direction with the OTF in the Fourier domain:

$$\hat{g}^{(\underline{m})}\left(\vec{q}_j\right) = \sum_{p} a_{\underline{m}p} \hat{g}\left(\vec{q}_j - k_{ax,p}\vec{e}_z\right) . \tag{20}$$

The sum over p passes through all OTF copies, shifted by illumination expansion wavevectors with the same lateral spatial frequency component $\vec{k}_{\underline{m}}$ and different axial component $k_{ax,p}\vec{e}_z$. $a_{\underline{m}p}$ are the corresponding illumination Fourier-order amplitudes. In this representation the illumination Fourier coefficients are thus absorbed in the definition of the order dependent OTFs. We can also make the filtering operation dependent on Fourier order by using different kernels $\hat{K}^{(\underline{m})}(\vec{q})$ for different Fourier orders m. In that case the general form of the super-resolution OTF becomes

$$\hat{g}^{SR}(\vec{q}) = \sum_{\underline{m}} \hat{K}^{(\underline{m})}(\vec{q} + \vec{k}_{\underline{m}})\hat{g}^{(\underline{m})}(\vec{q} + \vec{k}_{\underline{m}}). \tag{21}$$

The previously considered case is retrieved if we choose $\hat{K}^{(\underline{m})}(\vec{q}) = w_m \hat{K}(\vec{q})$, meaning that all kernels are equal up to the weighting factors w_m.

For the case of FDR the symmetric equation $\hat{K}^{(\underline{m})}(\vec{q}) = \hat{g}^{(\underline{m})}(\vec{q})$ still holds [14,16].

For the case of SDR we will use the expression for the SIM reconstruction:

$$I^{SR}(\vec{r}) = \sum_{r=1}^{M_r} \sum_{n=1}^{M_t} \sum_{\underline{m}} \exp(2\pi i \vec{k}_{r\underline{m}} \cdot (\vec{r} - \vec{u}_{rn}))(K^{(\underline{m})}(\vec{r}) \otimes I^{rn}(\vec{r}) \,. \tag{22}$$

In practice, it only makes sense to use different $K^{(\underline{m})}$ for different transfer functions $g^{(\underline{m})}$, which means that the expression (22) naturally splits into two different sums over r and n for the conventional SIM with a woodpile illumination pattern: one for the orders 0, ±2 and another for the orders ±1.

Recently another variant of 3D SIM setups has emerged [29]. In this another modality, multiplane acquisition [31–33] and trans-illumination [34] are combined to allow for a faster acquisition rate. Crucially, in the corresponding reconstruction procedure all displaced OTF copies are separated, and hence only one kernel type is required.

Research Article Vol. 34, No. 12 / 15 Jun 2026 / Optics Express 22946
Optics EXPRESS

3. Spectral signal-to-noise ratio

3.1. General expressions

The SSNR calculations provided in [16] will here be generalized to the case of an arbitrary linear reconstruction by replacing the OTF-based low-pass filters $g^{(\underline{m})}$ with arbitrary kernels $K^{(\underline{m})}$. The signal power S and the noise power N of an arbitrary SIM reconstruction are following Eq. (22)

$$\hat{S}(\vec{q}_j) = \left| \sum_{\underline{m}} \hat{K}^{(\underline{m})}(\vec{q}_j + \vec{k}_{\underline{m}}) \hat{g}^{(\underline{m})}(\vec{q}_j + \vec{k}_{\underline{m}}) \right|^2 |\hat{f}(\vec{q}_j)|^2, \tag{23}$$

$$\begin{aligned} \hat{N}(\vec{q}_j) = &\sum_{\underline{m},\underline{m}'} \hat{K}^{(\underline{m})}(\vec{q}_j + \vec{k}_{\underline{m}}) \hat{K}^{(\underline{m}')*}(\vec{q}_j + \vec{k}_{\underline{m}'}) \hat{g}^{(\underline{m}-\underline{m}')}(\vec{k}_{\underline{m}} - \vec{k}_{\underline{m}'}) \hat{f}(\vec{0}) \\ &+ N\sigma^2 \sum_{\underline{m}} |\hat{K}^{(\underline{m})}(\vec{q}_j + \vec{k}_{\underline{m}})|^2. \end{aligned} \tag{24}$$

The first term in the sum for the noise power corresponds to the shot noise and the second to the readout noise, with the readout noise variance σ^2. In the approximation $\hat{g}(\vec{k}_{\underline{m}} - \vec{k}_{\underline{m}'}) \ll \hat{g}(\vec{0}) = 1$, which is valid in case the orders in Fourier space have a relatively large separation, the noise power simplifies to

$$\hat{N}(\vec{q}_j) = \sum_{\underline{m}} |\hat{K}^{(\underline{m})}(\vec{q}_j + \vec{k}_{\underline{m}})|^2 (\hat{f}(\vec{0}) + N\sigma^2) \,. \tag{25}$$

In this approximation, the SSNR factorizes into a kernel-dependent part and an object-dependent part, as

$$SSNR(\vec{q}_j) = \frac{\left| \sum_{\underline{m}} \hat{K}^{(\underline{m})}(\vec{q}_j + \vec{k}_{\underline{m}})^* \hat{g}^{(\underline{m})}(\vec{q}_j + \vec{k}_{\underline{m}}) \right|^2}{\sum_{\underline{m}} |\hat{K}^{(\underline{m})}(\vec{q}_j + \vec{k}_{\underline{m}})|^2} \frac{|\hat{f}(\vec{q}_j)|^2}{\hat{f}(\vec{0}) + N\sigma^2} \,. \tag{26}$$

The kernel part, which we call in this work $SSNR_K(\vec{q}_j)$, is the first factor in the above product

$$SSNR_K(\vec{q}_j) \equiv \frac{\left| \sum_{\underline{m}} \hat{K}^{(\underline{m})}(\vec{q}_j + \vec{k}_{\underline{m}})^* \hat{g}^{(\underline{m})}(\vec{q}_j + \vec{k}_{\underline{m}}) \right|^2}{\sum_{\underline{m}} |\hat{K}^{(\underline{m})}(\vec{q}_j + \vec{k}_{\underline{m}})|^2} \,. \tag{27}$$

3.2. Optimality of the least-squares reconstruction

In the following we provide the proof that the choice $\hat{K}^{(\underline{m})}(\vec{q}_j) = \hat{g}^{(\underline{m})}(\vec{q}_j)$, corresponding to the least-squares motivated FDR, gives the best possible $SSNR(\vec{q}_j)$ reconstruction for all spatial frequencies $\vec{q}_j$.

If we define a complex-valued vector field as $\tilde{A}(\vec{q}_j) \equiv \{\hat{A}^{(\underline{m}_1)}(\vec{q}_j), \hat{A}^{(\underline{m}_2)}(\vec{q}_j), \ldots \hat{A}^{(\underline{m}_M)}(\vec{q}_j)\}$, we can introduce a scalar product

$$\langle \tilde{A} | \tilde{B} \rangle (\vec{q}_j) = \sum_{\underline{m}} \hat{A}^{(\underline{m})}(\vec{q}_j)^* \hat{B}^{(\underline{m})}(\vec{q}_j) \,. \tag{28}$$

With this scalar product the kernel dependent SSNR factor can be written in compact form as:

$$SSNR_K(\vec{q}_j) = \frac{\left| \langle \hat{K} | \hat{g} \rangle (\vec{q}_j) \right|^2}{\langle \hat{K} | \hat{K} \rangle (\vec{q}_j)} \,. \tag{29}$$

where in this section we redefine the shifted kernel and OTF copies $\hat{K}^{(\underline{m})}(\vec{q}+\vec{k}_{\underline{m}})$ and $\hat{g}^{(\underline{m})}(\vec{q}+\vec{k}_{\underline{m}})$ as $\hat{K}^{(\underline{m})}(\vec{q})$ and $\hat{g}^{(\underline{m})}(\vec{q})$ for convenience. For the least-squares FDR reconstruction $\hat{K}^{(\underline{m})}(\vec{q}_j) = \hat{g}^{(\underline{m})}(\vec{q}_j)$

Optics EXPRESS

and we find that

$$SSNR_{K,LS-FDR}(\vec{q}_j) = \frac{\left|\langle\hat{g}|\hat{g}\rangle(\vec{q}_j)\right|^2}{\langle\hat{g}|\hat{g}\rangle(\vec{q}_j)} = \langle\hat{g}|\hat{g}\rangle(\vec{q}_j)\,. \tag{30}$$

Taking the ratio between the kernel dependent SSNR factors for the general case and the least squares case, and subsequently applying Cauchy's theorem to the ratio, gives

$$\frac{SSNR_K(\vec{q}_j)}{SSNR_{K,LS-FDR}(\vec{q}_j)} = \frac{\left|\langle\hat{K}|\hat{g}\rangle(\vec{q}_j)\right|^2}{\langle\hat{K}|\hat{K}\rangle(\vec{q}_j)\langle\hat{g}|\hat{g}\rangle(\vec{q}_j)} \leq 1 \tag{31}$$

which proves the statement. This theorem is the key theoretical result of this paper, and we will use it subsequently to quantify the optimality of SIM reconstructions.

The result of Eq. (31) can be interpreted as following from the addition of Gaussian random variables. By inversion of the SIM phase matrix, one obtains separated spatial frequency bands $\hat{g}^{(\underline{m})}(\vec{q}+\vec{k}_{\underline{m}})\hat{f}(\vec{q})$, which can be considered independent noisy measurements of the object $\hat{f}(\vec{q})$. The result (31) is then the optimal guess of the ground truth [15].

The theorem can be generalized to cases where the image Fourier orders have an arbitrary separation, so that the OTF factors $\hat{g}(\vec{k}_{\underline{m}} - \vec{k}_{\underline{m}'})$ are not necessarily small (see Supplement 1 for proof). This generalized SSNR optimality theorem can also be used to quantitatively assess the error induced by the approximation of large order separation. It turns out that for practical 2D and 3D SIM cases, which typically have a fine illumination pattern pitch, this error is at the few percent level or less.

3.3. Comparison to SDR

For the SDR case $\hat{K}^{(\underline{m})}(\vec{q}_j) = 1$ it follows that

$$SSNR_{K,SDR}(\vec{q}_j) = \frac{1}{M}\left|\sum_{\underline{m}} \hat{g}^{(\underline{m})}(\vec{q}_j + \vec{k}_{\underline{m}})\right|^2 . \tag{32}$$

In case the overlap between orders for a spatial frequency $\vec{q}_j$ is small, we may approximate this as:

$$SSNR_{K,SDR}(\vec{q}_j) \approx \frac{1}{M}\sum_{\underline{m}} \left|\hat{g}^{(\underline{m})}(\vec{q}_j + \vec{k}_{\underline{m}})\right|^2 . \tag{33}$$

which is a factor M, the number of Fourier orders, smaller than the optimal case. So, the larger the number of harmonics in the illumination expansion, the worse the choice of this trivial kernel. We have for the conventional two-wave 2D-SIM configuration $M = 3$, for the three-wave 3D-SIM configuration $M = 5$, and for the lattice SIM configurations M can easily grow more than 10 times [14], making the simplistic SDR scheme substantially sub-optimal.

3.4. Theoretical restriction on finite kernels

From our key result Eq. (31) it follows that the best kernel for a real-space reconstruction is equal to the PSF. However, the PSF is unbounded in real space, which makes it impossible to precisely implement the real-space convolution operation with a physical PSF in a reasonable time (it can, however, be possible for special cases of unbounded approximate PSF models, such as the Gaussian PSF model, which allow for a recursive implementation of the filtering operation [35]). In this subsection, we show how we can select small real-space kernels $\hat{K}^{(\underline{m})}(\vec{q}_j)$ that result in a SSNR approaching the optimal SSNR of the least-squares motivated FDR, but can nevertheless be computed fast.

Optics EXPRESS

From the comparison between SDR and FDR in the previous subsection and the general shape of SSNR Eq. (27), we can make an educated guess on the shape of the kernels, which leads to reconstructions with high SSNR. One can see that both the nominator and the denominator of Eq. (27) contain sums over illumination Fourier orders $\underline{m}$. In the previous subsection, we showed that the SSNR for the naive SDR reconstruction was poor due to the factor M coming from the denominator. Meanwhile, the nominator was reduced to the case of the FDR reconstruction due to the small overlap between different orders. Our intuition is that if the overlap between orders in the denominator is also small, then we will arrive at approximately the same SSNR ratio as in the case of FDR. Indeed, in the limit of small overlaps, we can split the fraction of sums into the sum of fractions,

$$\frac{\left|\sum_{\underline{m}} \hat{K}^{(\underline{m})}(\vec{q}_j+\vec{k}_{\underline{m}})^* \hat{g}^{(\underline{m})}(\vec{q}_j+\vec{k}_{\underline{m}})\right|^2}{\sum_{\underline{m}} |\hat{K}^{(\underline{m})}(\vec{q}_j+\vec{k}_{\underline{m}})|^2} \sim \sum_{\underline{m}} \frac{\left|\hat{K}^{(\underline{m})}(\vec{q}_j+\vec{k}_{\underline{m}})^* \hat{g}^{(\underline{m})}(\vec{q}_j+\vec{k}_{\underline{m}})\right|^2}{|\hat{K}^{(\underline{m})}(\vec{q}_j+\vec{k}_{\underline{m}})|^2} = \sum_{\underline{m}} \left|\hat{g}^{(\underline{m})}(\vec{q}_j+\vec{k}_{\underline{m}})\right|^2 . \tag{34}$$

We emphasize that "small" in our overlap estimation does not refer to the size of the area of overlap in the Fourier domain, but the effective ratio $\hat{g}^{(\underline{m})}(\vec{q}_j+\vec{k}_{\underline{m}})/\hat{g}^{(\underline{m})}(\vec{q}_j+\vec{k}_{\underline{m}}^{\text{nearest}})$, where $\vec{k}_{\underline{m}}^{\text{nearest}}$ means that $||\vec{k}_{\underline{m}}^{\text{nearest}}+\vec{q}_j|| \leq ||\vec{k}_{\underline{m}}+\vec{q}_j||$. In other words, we want nearly all signal and noise at nearly each spatial frequency to come from a single Fourier order.

The reason why SSNR optimization essentially boils down to noise reduction can be understood as follows: signal transfer for each order is band-limited and becomes small near the edge of the band, while the noise each band receives in the absence of filtering is approximately white and band-unlimited. Thus, each sum over orders only adds up signal from one or a couple of overlapping bands, but at the same time adds up noise from each band (hence the factor M in the subsection above). This implies that the shape of the kernel is relatively unimportant for the resulting SSNR, so far the kernel has approximately the same effective size in the Fourier domain as the OTF.

This argument and computational performance considerations impose the following requirements on the kernel for real-space SIM reconstruction. First, the support of $K(\vec{r}_j)$ in real space must be as small as possible to allow fast computations. Second, its Fourier transform should have similar (approximate) support as the optical transfer function to reduce the out-of-band noise. Finally, we want $|\hat{K}(\vec{q}_j)|>0$ if $\hat{g}(\vec{q}_j)>0$, as otherwise there is zero signal transfer at some spatial frequencies. In this work, we show that it is possible to select $\hat{K}(\vec{q}_j)$ to be real and impose even a stricter requirement $\hat{K}(\vec{q}_j) \geq 0$ everywhere to avoid any possibility of the signal from different bands to add up to 0 in the case of a significant band overlap.

3.5. Practical finite kernels

The criteria from Section 3.4 enable a closed-form solution of the kernel function $K(\vec{r}_j)$ given the support of the kernel in real space. This follows the same line of reasoning as applied in Ref. [17] in the context of optimal transfer functions for band-limiting imaging. The narrowest non-negative image $\hat{O}(\vec{q}_j)$ in the Fourier domain is given by a function $O(\vec{r})$, which can be represented as an autoconvolution of another function with itself $O(\vec{r}) = o(\vec{r}) \otimes o(\vec{r})^*$. The stated criteria then imply that the real space kernel function should have the same functional dependence on spatial coordinates as the dependence of the incoherent OTF on spatial frequencies! The role of the pupil function in the current context is taken up by the function $o(\vec{r})$. The solution for the cases of one dimension is:

$$o(r) = \Pi(2r/r^{\text{eff}}) \quad \text{and} \quad O(r) = \Lambda(r/r^{\text{eff}}), \tag{35}$$

where Π and Λ are symbols for the common rectangular and triangular functions, respectively, and r^{eff} is a scaling parameter that measures the support of the kernel function in real space. In two dimensions, we find:

$$o(\vec{r}) = \Pi(2|\vec{r}|/r^{\text{eff}}) \quad \text{and} \quad O(\vec{r}) = H\left(\frac{|\vec{r}|}{r^{\text{eff}}}\right) \tag{36}$$

with:

$$H(x) = \frac{2}{\pi}\left[\cos^{-1}(x) - x\sqrt{1-x^2}\right], \tag{37}$$

where again r^{eff} is a scaling parameter that measures the support of the kernel function in real space.

We now need to estimate the kernel size in the discrete pixelized case. Based on the theory of this section, we expect the optimal *SSNR* performance when the OTF and the effective kernel size in the Fourier domain match. Therefore, a good choice for the scaling parameter r^{eff} is r_0 such that the first zero of the kernel $\hat{K}(\vec{q}_j)$ coincides with the cut-off of the OTF $\hat{g}(\vec{q})$ at spatial frequency $|\vec{q}_c| = 2NA/\lambda$. In one dimension this implies:

$$K(q) = \text{sinc}\left(r_0\frac{2NA}{\lambda}\right)^2 = 0 \tag{38}$$

giving $r_0 = \lambda/2NA$. Thus, a one dimensional kernel must have a width $2r_0$ equal to 4 pixels of the acquired images in case of Nyquist sampling (pixel size equal to $\lambda/4NA$). When the filter is applied after the typical 2× upsampling needed for the final SIM reconstruction the width is 8 super-resolution pixels. It appears to be advantageous to use an odd number of pixels, that is to sample the kernel in a way such that the central pixel corresponds to $\vec{q}_j = 0$. Then the last pixels from both sides can be omitted as they are already sampled at zero value. Therefore, a real-space zero-centered finite kernel can have the size of just 7×7 super-resolution pixels. In the same way, in two dimensions, it is possible to obtain for the kernel size an estimate of 9×9 pixels.

Following the discussion above, we can introduce a convenient dimensionless measure for the kernel size as $s = r^0/r_{\text{eff}}$. This value s is a generalization of the kernel size to the continuous domain: while computationally the kernel is still sampled at several points, the values of these points differ, making it possible to distinguish between kernels with the same number of pixels (in so far that number is greater than 1). This size measure is sampling-independent, being instead determined by the physical quantity (the OTF size). Conveniently, optimal filtering performance is expected when $s = 1$.

The step to 3D kernels appears to be rather intricate, as the function of the filtering step is twofold. First, it must have the character of low-pass filtering, to reduce noise where there is no signal. Second, the filter must also provide good sectioning by suppressing axial crosstalk. As the lateral extent of the ideal case kernel in real space (which is just the 3D PSF) grows with axial separation a finite size real space kernel will always fall short in accurately mimicking the ideal case. This originates from the non-convex shape of the 3D OTF due the missing cone. The consequence is that the relative reduction in SSNR compared to the ideal case can be expected to be somewhat larger than for the 2D case. Moreover, any real dataset consists of a finite number of layers, giving an axial streak in Fourier space because of the assumed periodic boundary conditions of the Fourier Transform. These spatial frequency components close to the axis $q_x = q_y = 0$ in spatial frequency space fill the missing cone region and are conveniently filtered out for the ideal case of low-pass filtering with the 3D OTF.

The solution we have found to meet both criteria is derived from earlier ideas to add notch filtering in addition to the low-pass filtering with the OTF [36,37]. This provides a degree of optical sectioning by suppressing the axial streaks in the image Fourier orders before placing the orders at the right location in Fourier space, albeit at the expense of a reduction in SSNR [16]. Usually, the notch factor is taken to be a Gaussian ‘dip’, with adjustable width and dip level. It

Optics EXPRESS

appears in practice that a width comparable to the OTF width and a dip level close to one gives a reasonable outcome. A kernel with finite size in real space mimicking this behavior is:

$$O\left(\vec{r}\right) = H\left(\frac{|\vec{r}|}{r^{\mathrm{eff}}}\right) - H\left(\frac{|\vec{r}|}{r^{\mathrm{eff}}}\right) \otimes H\left(\frac{|\vec{r}|}{r^{\mathrm{eff}}}\right), \tag{39}$$

which gives the Fourier space filter function:

$$\hat{O}\left(\vec{q}\right) = A\left(r^{\mathrm{eff}}\left|\vec{q}\right|\right) - A\left(r^{\mathrm{eff}}\left|\vec{q}\right|\right)^2 = A\left(r^{\mathrm{eff}}\left|\vec{q}\right|\right)\left[1 - A\left(r^{\mathrm{eff}}\left|\vec{q}\right|\right)\right], \tag{40}$$

with the Airy distribution function:

$$A\left(x\right) = \left[\frac{2J_1\left(2\pi x\right)}{2\pi x}\right]^2. \tag{41}$$

Equation (39) has a support in real space that is twice as big as the Airy kernel of Eq. (36), but still finite, and the Fourier space filter of Eq. (39) clearly factorizes in a low-pass filter and a notch filter.

A variant of the above filter explicitly includes the axial dimension. It is then attractive to use a separable kernel $O(\vec{r}) = K_l(x, y)K_a(z)$. The obvious choice then for the lateral part is the above Airy notch filter, and for the axial part the sinc type filter. This is advantageous for two reasons. First, it is computationally favorable to convolve in the lateral and axial directions separately instead of in a non-separable way, as this significantly reduces the number of operations per pixel significantly. Second, the axial filter can be adapted to the Fourier order, because the 1st order for the conventional woodpile pattern illumination has an axially split support in Fourier space, different from the 0th and 2nd orders. Thus, only the $K_a(z)$ part must be changed. The lateral and axial kernel size can now be defined by two dimensionless parameters s_l and s_a, respectively. In principle, they can be chosen independently, in practice it appears that both are optimum close to $s_l = 1$ and $s_a = 1$, in agreement with the above line of reasoning. This points to another advantage of this measure as opposed to some characteristic real-space size, such as Airy units or r_0. Namely, it provides a possibility to unify the drastically different behavior of the widefield PSF and OTF in the lateral and axial directions, and instead make use of the fact that in both the lateral and axial directions the OTF is band-limited with the lateral cut-off frequency [LCF] equal to $2NA/\lambda$ and the axial cut-off frequency [ACF] equal to $(1 - n\cos\alpha)/\lambda$.

4. Simulation results

In this section, we provide the results of simulations for 2D and 3D reconstructions for conventional and lattice SIM. In our simulations we consider the following SIM configurations: conventional stripe pattern, square lattice with four linearly polarized obliquely incident plane waves and also lattice configurations with hexagonal symmetry. In the case of 2D SIM, hexagonal symmetry is achieved with three obliquely incident plane waves [38], while in the case of 3D SIM seven waves are required [14]. All parameters for 3D configurations coincide with those found to be optimal in [14]. We use a linearly polarized normally incident plane wave for the 3D configuration with square symmetry, and a circularly polarized normally incident wave for the 3D configuration with hexagonal symmetry.

We use a high-NA and vectorial PSF model for a freely rotating emitter [39] for the forward model. The NA of the lens is taken to be 1.43 with the refraction indices of the sample and the immersion medium are both set to 1.5 for the sake of simulation simplicity. The angle of incidence of the obliquely incident plane waves is selected to produce a theoretical resolution improvement of 1.9 times the diffraction limit.

Optics EXPRESS

As a measure of reconstruction quality, we not only consider the SSNR ratio metric we introduced in section 3 but also the measures of SSNR entropy and SSNR volume we have introduced before [14]. These are defined as:

$$SSNR_{K,V} = \sum_{j=1}^{N^2} SSNR_K(\vec{q}_j)\,. \tag{42}$$

$$SSNR_{K,S} = -\sum_{j=1}^{N^2} \frac{SSNR_K(\vec{q}_j)}{SSNR_{K,V}} \log \frac{SSNR_K(\vec{q}_j)}{SSNR_{K,V}}\,. \tag{43}$$

The SSNR volume $SSNR_{K,V}$ measures the total amount of transferred "useful signal", while the SSNR entropy $SSNR_{K,S}$ accounts for the distribution of the signal over spatial frequencies [14]. An increase in any of these functions without a change in another signifies an improvement in the reconstruction procedure. Due to the complexity of the SIM super-resolution transfer function, $SSNR_{K,S}$ and $SSNR_{K,V}$ may have a different dependence on the reconstruction parameter at hand.

In Fig. 1 we provide a comparison of the object-independent part of the SSNR for 2D-SIM reconstructions. Panels (a-c) show the ring averaged $SSNR_K$ for the two-dimensional reconstructions with a varying discrete kernel size of 1, 5, and 9 pixels correspondingly. Panels (d-f) show the ratio of the $SSNR_K$ to the ideal $SSNR_K$ of the two-dimensional least squares FDR for a conventional stripe configuration. The results confirm that in the 2D case a nearly ideal SSNR can be achieved with a 9×9 px kernel everywhere in the non-zero signal transfer region, while a choice of the trivial 1×1 px kernel significantly reduces useful signal transport outside of the widefield OTF support.

In Fig. 2 we show a more general comparison of the same 2D configurations. In panels (a) and (b), we show the dependence of the SSNR entropy and SSNR volume of different configurations on the lateral kernel size. It can be seen the optimal kernel factor s_l varies a bit depending on the measure, the kernel, and the configurations but in all cases s_l is found to be in the range 0.8-0.95, just a bit smaller than a theoretically motivated value of 1. We see that the volume-entropy method can be used to fine-tune the optimal kernel size depending on a number of parameters. For clarity, in this work, we will stick to a value $s_l = 1$, which results in a marginally worse SSNR, and the difference is typically unobservable. We notice that small s_l factors resulting in a kernel size 1px - that is, a naive SDR reconstruction - show a significant reduction in SSNR volume and entropy, as expected. In contrast, the optimal s_l gives rise to SSNR measures at a level just a bit below the optimum least squares reconstruction. It appears that a radially symmetric kernel gives a bit better results than a triangular kernel (2D triangular kernel is a laterally separable kernel equal to the direct product of two one-dimensional triangular kernels).

At this point, it is appropriate to discuss the practically important case of the reconstruction in the presence of aberrations. In the conventional FDR reconstruction the reconstruction Fourier domain low-pass filter is typically taken to be the ideal OTF, while the physical OTF can suffer from some unknown aberrations. From the discussion in Section 3.4 and Fig. 2, it is expected that the precise shape of the reconstruction kernel does not matter that much, insofar out-of-band noise is properly removed. At the same time, aberrations of the physical OTF lead to a reduction in achievable SSNR as we showed in our earlier work [14].

In Fig. 3, we compare the ring-average SSNSR for 2D SIM reconstructions in different cases involving (non)-aberrated OTFs. First, we consider the cases of conventional FDR least-squares reconstruction (that is, when the reconstruction kernel is equal to the physical OTF) for the cases of ideal and aberrated transfer functions (labeled *II* and *AA*) respectively. Then we consider the practically relevant cases of an aberrated physical OTF and the reconstruction kernel equal to the ideal OTF (labeled *AI*) and of the real-space finite kernel reconstructions for the optimally selected OTF-like kernel ($s_l = 1$) (labeled *AK*). We consider these cases with different wavefront aberration strengths: a) 0.072λ and b) 0.144λ root mean square.

Research Article Vol. 34, No. 12 / 15 Jun 2026 / Optics Express 22952
Optics EXPRESS

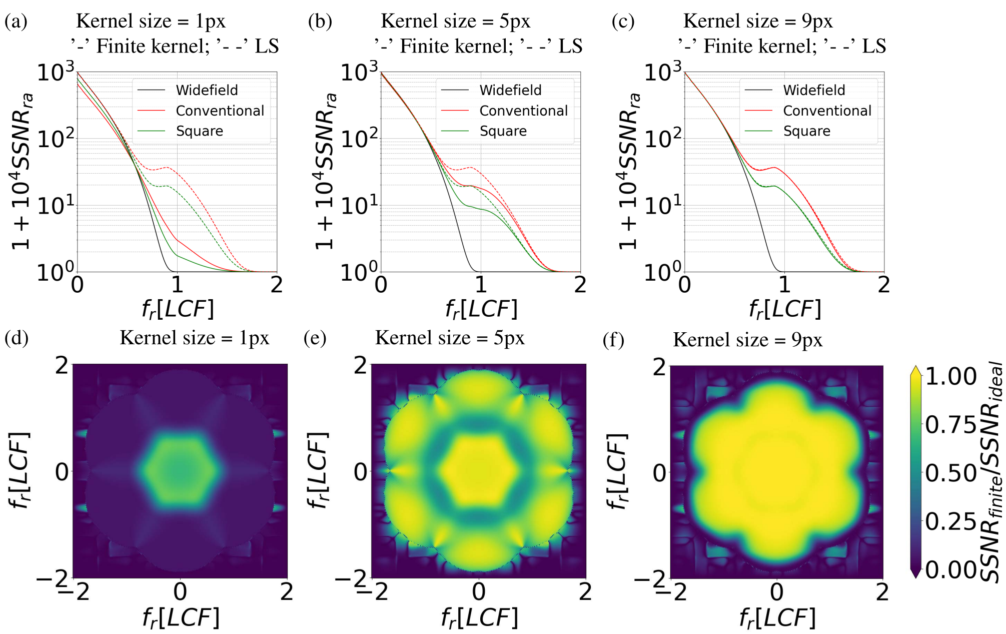

Fig. 1. Object independent $SSNR$ part ($SSNR_K$) and $SSNR_K$ ratios for 2D SIM reconstructions with different finite kernel sizes. (a-c) Ring averaged $SSNR_K$ for the kernel size 1, 5 and 9 pixels respectively. LCF: lateral cut-off frequency; ACF: axial cut-off frequency. Dashed lines "- -" indicate corresponding optimal $SSNR_K$ of the least-squares reconstructions. (d-f). Colormaps of the ratios of $SSNR_K$ of the final kernel reconstructions to the $SSNR_K$ of the optimal least-square reconstruction for the conventional SIM with 3 rotations.

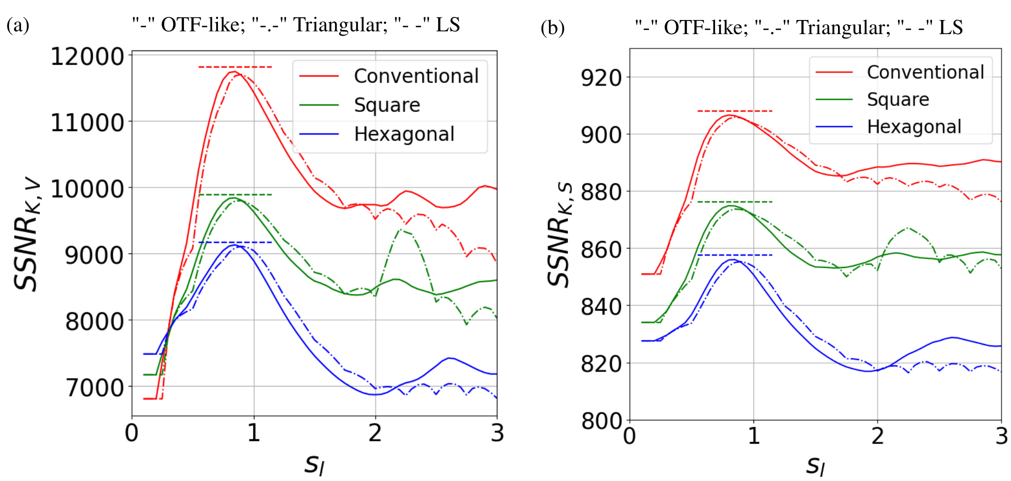

Fig. 2. Dependence of the SSNR a) volume and b) entropy for common 2D SIM configurations on the finite kernel size, expressed in the terms of the lateral kernel size factor s_l. Linestyles "-" and "-.-" denote SSNR measures for OTF-like radially symmetric and pyramidal kernels respectively. A small dashed segment "- -" shown over the curve peaks indicates the highest achievable least-squares SSNR measure values. "Conventional", "Square" and "Hexagonal" labels refer to the conventional two-waves SIM configuration, four-waves SIM configuration with square symmetry, and three-waves SIM configuration with hexagonal symmetry.

Optics EXPRESS

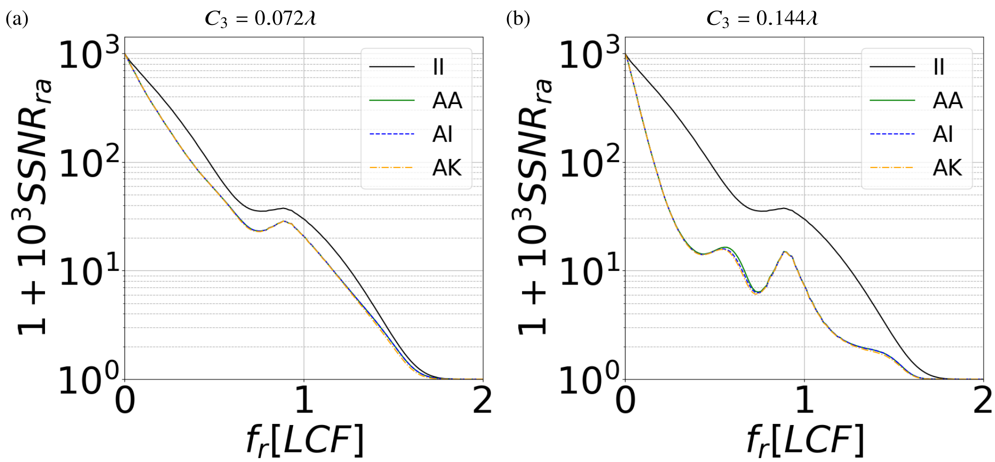

Fig. 3. Ring-averaged $SSNR_K$ for SIM reconstructions with the ideal OTF and spherically aberrated OTF and different reconstruction kernels. a) $C_3 = 0.072\lambda$. b) Aberration strength $C_3 = 0.144\lambda$. The two-letter abbreviations mean the following: the first letter corresponds to the physical OTF ("I" for ideal or "A" for aberrated); the second letter corresponds to the reconstruction kernel. "I" or "A" means that a conventional Fourier-domain reconstruction with the kernel equal to the Ideal or Aberrated OTF was used, whereas "K" denotes a real-space reconstruction with a finite real-space OTF-like kernel of optimal size $s_l = 1$.

It is seen that the SSNR curves are split based on the physical OTF. The presence of aberrations reduces the SSNR. The Cauchy theorem (31) imposes the upper bound on the SSNR in the presence of aberrations (AA-curve). However, since other reconstruction kernels have the same effective size and remove out-of-band noise efficiently, the reduction in the SSNR in these reconstructions is negligible compared to the highest possible value.

In Fig. 4 we show an example of 2D-SIM reconstructions for simulated line data. The average photon count is 431 photon/px. In this figure, one can see the dependence of contrast and noise level of the reconstructions on the chosen kernel. The widefield result (b) gives a blurry representation of the ground truth object (a). The optimum least squares FDR (c) produces an image that is clean from noise yet blurry, which can be further optimized by means of Wiener filtering to the extent shown in (d). The naive SDR with a trivial kernel (no low-pass filtering at all) (e) produces an image very similar to the widefield case (b), because high frequent noise is not suppressed at all. A reconstruction with an OTF-like finite kernel with an optimal size factor $s_l = 1$ (f) also produces an image with strongly reduced noise, but at a contrast level that is improved compared to the FDR case before Wiener filtering. This makes the SDR reconstruction preferable in the case Wiener filtering is challenging for any reason (for example, variable imaging conditions across the FOV).

We advance to a more challenging case of 3D reconstructions. Figure 5 shows similar metrics to those used in the 2D case. Here we use a fully separable 3D kernel, which can be computed as a direct product of a lateral 2D OTF-like kernel and an axial 1D triangular kernel, (see Section 3.4). The kernels for the Fourier orders -1 and 1 are computed to match the physical transfer function given by Eq. (20): a weighted sum of the positively and negatively axially displaced OTF copies. Panels (a-c) show the ratio of the ring averaged $SSNR_K$ with an optimal finite kernel size to the ideal $SSNR_K$ for a 3-dimensional reconstruction for the conventional configuration, the 5-waves configuration with square symmetry, and the 7-waves configuration with hexagonal symmetry correspondingly. One can see that the difference with the 2D-case is that albeit high SSNR is achieved almost everywhere within SIM non-zero transfer region, there is a small region

Optics EXPRESS

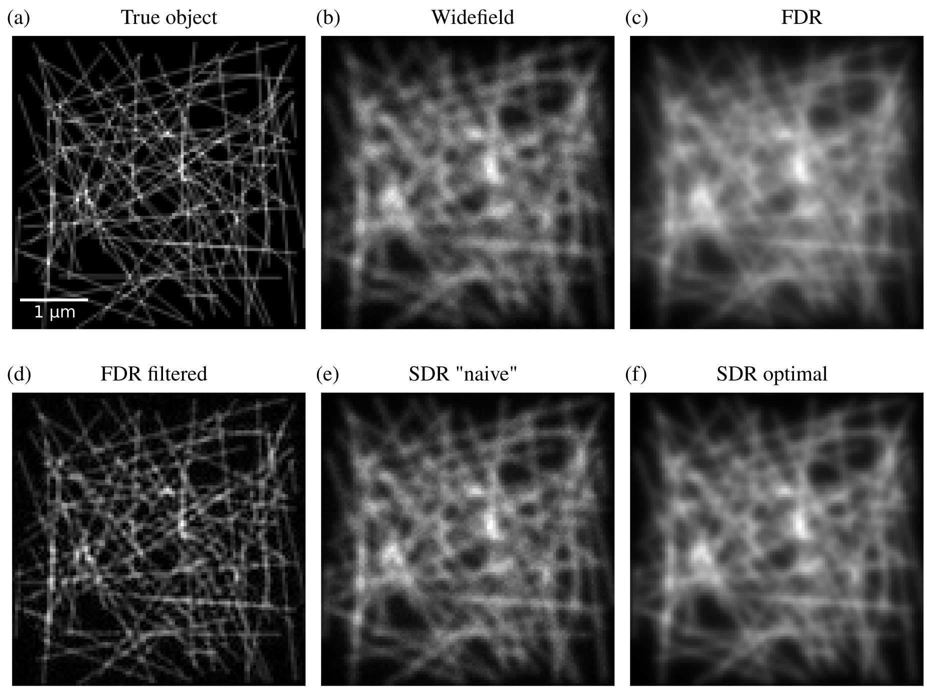

Fig. 4. SIM Reconstructions of simulated 2D lines. Simulation wavelength $\lambda = 488nm$. a) Simulated object. b) Widefield image. c) Least-squares FDR reconstruction. d) State-of-art SIM least-squares reconstruction with contrast optimization by the means of true Wiener filtering [16]. e) SDR with trivial kernel (no low-pass filtering). f) SDR with an optimal 9 pixels OTF-like kernel. No contrast optimization is applied in panels (c, e, f).

right above the zero frequency, where the SSNR transfer is significantly reduced. As expected, the complex shape of the OTF in the z-direction cannot be fully mimicked by a small finite kernel. Interestingly, high spatial frequencies, which are typically those of primary interest, show the $SSNR_K$ comparable to the ideal reconstruction.

Deconvolution procedures such as Wiener filtering will suppress spatial frequencies where $SSNR(\vec{q}_j)<1$ while leaving nearly unchanged those spatial frequencies with high SSNR [16]. The total $SSNR$ is the product of the object frequency and the kernel-dependent part, Eq. (26). Spatial frequency content in natural images tends to decrease with an increasing value of a spatial frequency vector $\vec{q}_j$ [40]. Thus, we expect the SSNR gap in the region of low frequencies to be largely compensated for by the large amount of signal within this region for thick samples. However, the optical sectioning is overall reduced.

Panels (d) and (e) show the colormap of the SSNR volume and entropy for the conventional stripe 3D SIM depending on the lateral kernel size factor s_l and the axial factor s_a. Interestingly, the results do not agree well with each other, which shows the complexity of the SSNR structure in 3 dimensions. While the SSNR volume is peaked around the axial factor $s_a = 1.1$ and the lateral factor $s_l = 1.2$, in line with the theoretical predictions, SSNR entropy favors an axial factor < 0.5, equivalent in the simulation to the kernel size of 1 px. In this case, there is no modulation in z-direction. Thus, the distribution of signal over spatial frequencies is, in some sense, more even, with only lateral modulation present, albeit at the price of the significant SSNR volume reduction.

This hints at the possibility of a computationally attractive case, in which a 2D kernel is used to perform a 3D reconstruction. We expect that computation acceleration can be achieved

Optics EXPRESS

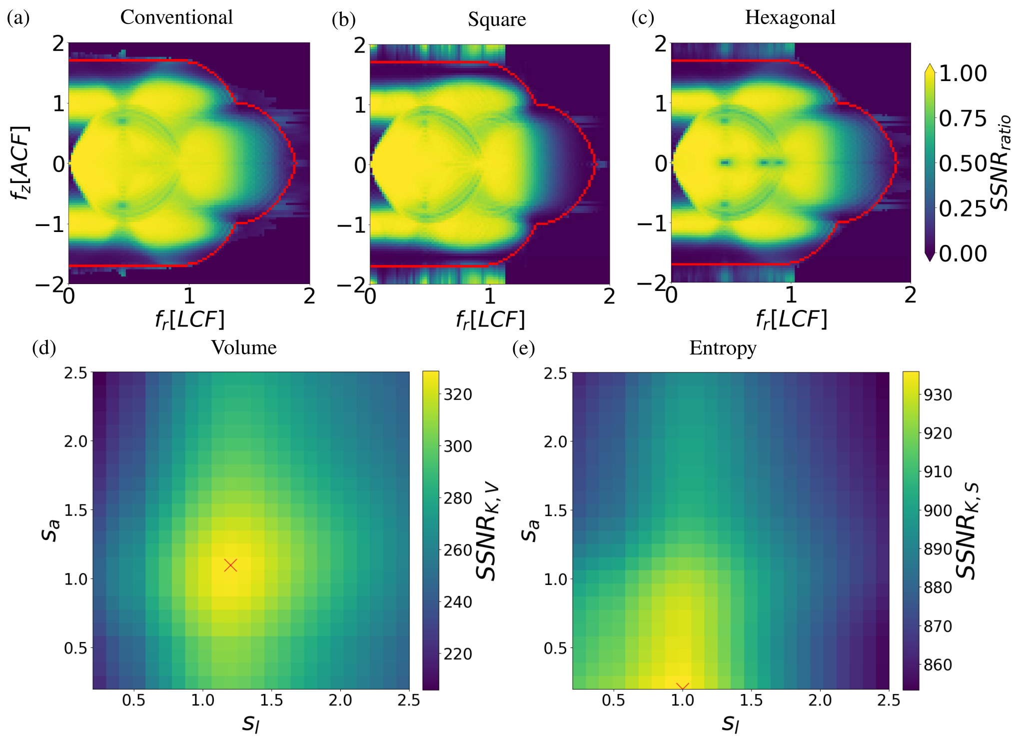

Fig. 5. Object independent *SSNR* part ($SSNR_K$) for 3D SIM reconstructions with a fully separable triangular 3D kernel. In red: theoretical OTF support. (a-c). Colormaps of the ratios of the ring averaged $SSNR_K$ to the ring averaged $SSNR_K$ of the optimal least-square reconstruction for 3D versions of the same configurations. Kernel size factors are selected to be $s_a = s_l = 1$. (d-e) Colormaps of the SSNR volume and entropy for the conventional stripe three-waves SIM back-focal plane configuration depending on the lateral and axial kernel size factors s_a and s_l.

due to the possibility of processing several slices in parallel, as well as due to the reduction of theoretical complexity which scales with the number of slices N_z instead of $N_z \log N_z$ required by the Fourier transform. Moreover, in this case, the memory requirements are significantly reduced for large datasets. We notice that the limiting factor here is that Wiener filtering and apodization procedures must still be performed in the 3D Fourier domain.

In Fig. 6 the ratio of $SSNR_K$ of the finite kernel reconstructions to the $SSNR_K$ of the optimal least-square reconstruction is shown. In Fig. 6 (a) the reconstruction procedure is only modified with a replacement of the ideal 3D kernels with the same for all orders finite 2D OTF-like kernel. One can see that albeit lateral super-resolution is achieved, high axial spatial frequencies are not well transmitted. Thus, in this case, further modifications to the reconstruction procedure are required.

One possibility is to increase the higher-orders modulation parameters $w_{\underline{m}}$ introduced in Eq. (13) to suppress noise coming from the zeroth Fourier order, naturally having a significantly higher modulation than other orders. In Fig. 6 (b) we show the same ratio of ring-averaged $SSNR_K$ of the reconstruction with a 2D finite OTF-like kernel and high-order amplification $w_1 = 10a_1$ and $w_2 = 5a_2$. These numbers are obtained by optimization of the SSNR entropy measure $SSNR_{K,S}$, which grows with higher order modulation coefficients and reaches a plateau around these values (figure not shown). We see that the optical sectioning is mostly restored at

Optics EXPRESS

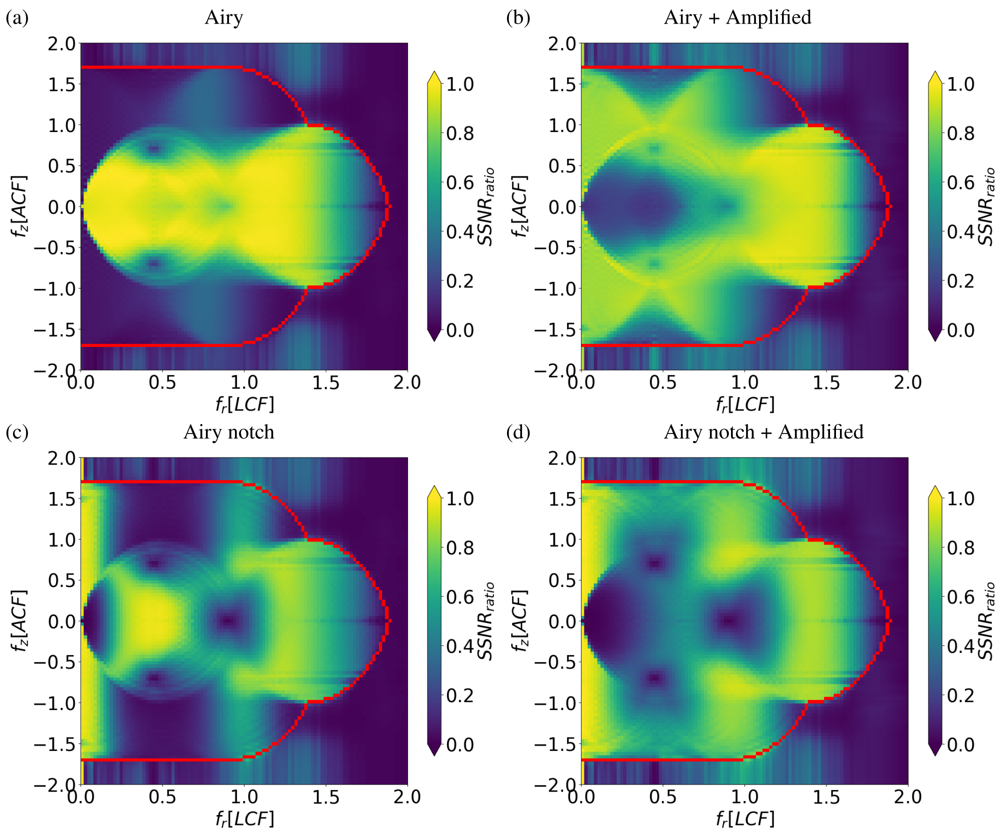

Fig. 6. Ratios of ring-averaged $SSNR_K$ of 3D SIM reconstructions for a conventional woodpile illumination pattern and a slice-by-slice reconstruction strategy with a 2D finite kernel to the optimal least-squares Fourier domain reconstruction. In red: theoretical 3D OTF support. (a) Reconstruction with the OTF-like kernel of the size $s = 1$. (b) Reconstruction with the same OTF-like kernel and amplified modulation coefficients $w_1 = 10a_1$ and $w_2 = 5a_2$. (c) Reconstruction with the Airy notch kernel, that has both low-pass and notch parts of the size $s = 1$. (d) Reconstruction with the same Airy notch kernel and amplified modulation coefficients $w_1 = 10a_1$ and $w_2 = 5a_2$.

the price of a decrease in the intermediate spatial frequency values in the region of support of the zeroth order OTF. Here again some SSNR trade-off is inevitable due to the complexity of the 3D OTF. However, for the same reasons as above, we expect that SSNR in this region remains much larger than one even though it is reduced compared to the optimum.

The applicability of this method is limited due to the presence of processing artifacts. As discussed in Section 3.5, the Fourier cross artifact results in the axial streaking in Fourier domain and hinders the subsequent contrast optimization. Therefore, instead of the low-pass kernels we have to consider Airy notch kernels, Eq. (40). In Fig. 6 (c) we show the ratio of $SSNR_K$ of the real-space reconstruction with this combined kernel to the $SSNR_K$ of the optimal least-square reconstruction. We see that the optical section on the optical axis is fully restored. Finally, in Fig. 6 (d) we show the reconstruction with the Airy notch kernel and simultaneous high Fourier order amplification. In comparison to the unmodulated case, high spatial frequency transfer is fully restored, resulting in a nearly ideal SSNR near the cut-off.

This finite notch-kernel approach is similar in spirit to that used in other SIM works to suppress the defocused background, for example, in a single-plane joint SDR [25]. The difference is that in our case we prioritize the SSNR increase and artifact reduction instead of the contrast optimization, which is achieved separately by means of Wiener filtering.

We use the strategy of simultaneous filtering with a combined Airy notch kernel and high Fourier order amplification for the experimental reconstructions in the following section.

5. Experimental results

We processed datasets we used earlier in Ref. [16]. First we considered 2D SIM reconstructions of a nanofabricated 2D test structure. We computed SIM reconstructions for both the standard ideal OTF filtering case, and for the real space finite support Airy filtering case. Both filtering apporaches were compared for two different types of reconstructions, namely the true Wiener and the flat-noise reconstructions proposed in Ref. [16]. These relate to the final Fourier space filtering step applied to the intermediate reconstruction of Eq. (6) to obtain the final SIM reconstruction. According to the true Wiener reconstruction we have:

$$\hat{I}^{SIM}\left(\vec{q}\right) = \hat{B}\left(\vec{q}\right) \frac{SSNR_{\mathrm{est}}\left(\vec{q}\right)}{1 + SSNR_{\mathrm{est}}\left(\vec{q}\right)} \frac{\hat{D}\left(\vec{q}\right)^{*}}{\left|\hat{D}\left(\vec{q}\right)\right|^{2} + \epsilon} \hat{I}^{SR}\left(\vec{q}\right), \tag{44}$$

with $\hat{B}\left(\vec{q}\right)$ the apodization function, typically a triangle shaped filter, to prevent excessive edge overshoot and negative pixel values [18], $SSNR_{\mathrm{est}}$ the estimated SSNR [16], and with:

$$\hat{D}\left(\vec{q}\right) = \sum_{\underline{m}} \hat{K}^{(\underline{m})}(\vec{q} + \vec{k}_{\underline{m}})\hat{g}^{(\underline{m})}(\vec{q} + \vec{k}_{\underline{m}}). \tag{45}$$

The number ϵ is on the order of the machine precision to prevent division by zero in regions outside the support of the OTF for SIM. The true Wiener reconstruction restores contrast and adjusts the level of regularization automatically to the estimated SSNR. According to the flat noise reconstruction we have:

$$\hat{I}^{SIM}\left(\vec{q}\right) = \frac{1}{\sqrt{\hat{N}\left(\vec{q}\right)}} \hat{I}^{SR}\left(\vec{q}\right), \tag{46}$$

with the noise power $\hat{N}\left(\vec{q}\right)$ defined in Eq. (24). The flat noise reconstruction has a uniform noise level throughout spatial frequency space so that the reconstruction reflects the physical SSNR level. Figure 7 shows the outcome of the comparison. On a qualitative level there is no recognizable difference between the ideal OTF filtering cases and the real space finite support Airy filtering cases, confirming the conclusions drawn from the simulation study. We have quantitatively confirmed this by a single image Fourier Ring Correlation (1FRC) analysis [41], indicating similar 1FRC resolution values for the OTF filtering and Airy filtering cases (125 nm, OTF filter + true Wiener; 105 nm, OTF filter + flat noise; 125 nm, Airy filter + true Wiener; 104 nm, Airy fiter + flat noise). There is a small difference between the true Wiener filtering cases and the flat noise filtering cases because of the low-pass filtering effect of the SSNR dependent regularization with true Wiener filtering.

Next, we considered single colour 3D SIM dataset of a tubulin sample and a two colour sampe of a C127 cell (further experimental details given in Ref. [16]). We compared true Wiener reconstructions with the default OTF filtering to the Airy notch filtering, both with and without an additional sinc-like low-pass filter in the axial spatial frequency direction (indicated as ‘Airy notch 3D’ and ‘Airy notch 2D’ filtering, respectively). For the Airy notch filtering cases the 1st and 2nd order modulation coefficients in the filters have been set to 10× and 5× the

Optics EXPRESS

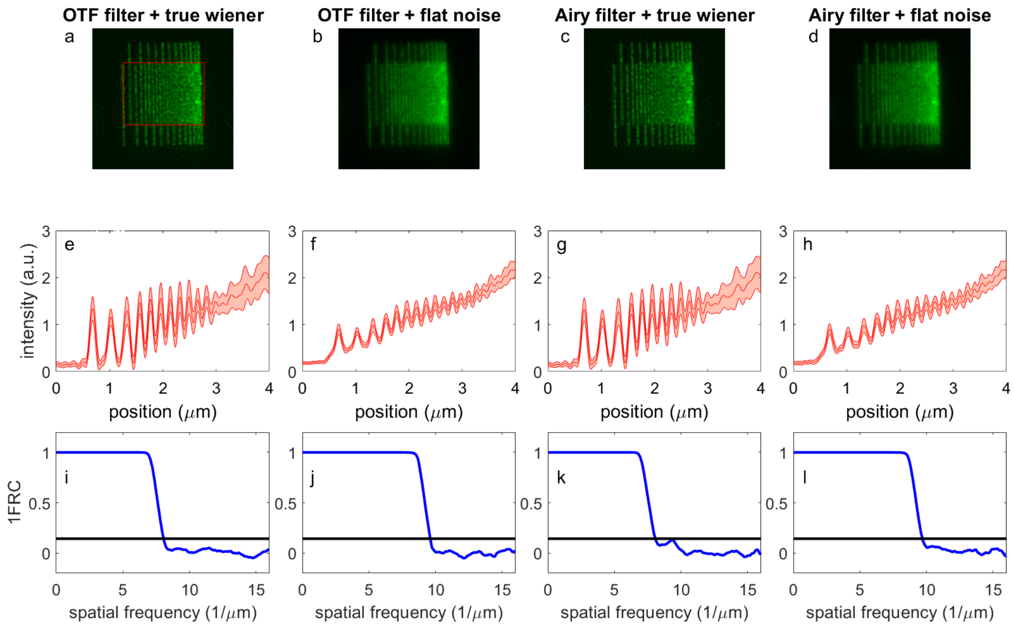

Fig. 7. 2D SIM reconstructions of a nanofabricated test structure. (a-d) Reconstructions for ideal OTF filtering and for real space finite support Airy filtering for true Wiener and flat noise reconstructions. (e-h) Cross-sections of line profiles averaged over rectangular area indicated in (a). (i-l) Single image FRC curves for the different filtering cases. The black line indicates the 1/7 threshold.

experimental values, respectively, following the settings used in our simulations. Figure 8 and Visualization 1 show the outcome for the tubulin sample. For this relatively sparse sample we find comparable reconstructions for all three cases, with a degree of sectioning that is slightly better for the Airy notch cases. This is due to the enhancement of the 1st order, which properly fills the missing cone in spatial frequency space. The measured SSNR for the Airy notch filtering cases is several orders of magnitude lower than for the OTF filtering case, but the reduction in the region of Fourier space with non-zero SSNR is very limited. The SSNR level for the Airy notch filtering cases at the lower spatial frequencies is still orders of magnitude higher than one, so that the visual appearance of the reconstruction remains satisfactory. Figure 9 and Visualization 2 show the outcome for the C127 cell dataset. For this less sparse sample we again find satisfactory reconstructions in all three cases. The SSNR of the notch filtering cases is substantially smaller than for the OTF filtering case, but the Fourier space region with non-zero SSNR is not compromised too much. The degree of sectioning is slightly better for the Airy notch cases, but a slight striping artefact can be seen in the Airy 2D notch case, which may be due to small imperfections in the illumination pattern parameter retrieval.

We have corroborated these conclusions with a quantitative analysis of single image Fourier Plane Correlation (1FPC), which combines the 1FRC method [41] with the 3D image resolution concept of FPC [42]. For the sparse tubulin sample we find similar 1FPC curves for the different filtering cases, in agreement with the similar image appearance and similar SSNR heatmaps. The 1FPC resolutions found are therefore also quite similar ($1FPC_{x,y,z}$ = 122, 123, 301 nm for OTF; $1FPC_{x,y,z}$ = 119, 119, 300 nm for Airy notch 3D; $1FPC_{x,y,z}$ = 119, 119, 300 nm for Airy notch 2D). The same conclusion holds for the green (H3K4me3) channel of the C127-cell dataset, where we find similar 1FPC curves and 1FPC resolutions ($1FPC_{x,y,z}$ = 127, 128, 377 nm for OTF; $1FPC_{x,y,z}$ = 130, 127, 358 nm for Airy notch 3D; $1FPC_{x,y,z}$ = 131, 129, 376 nm for Airy

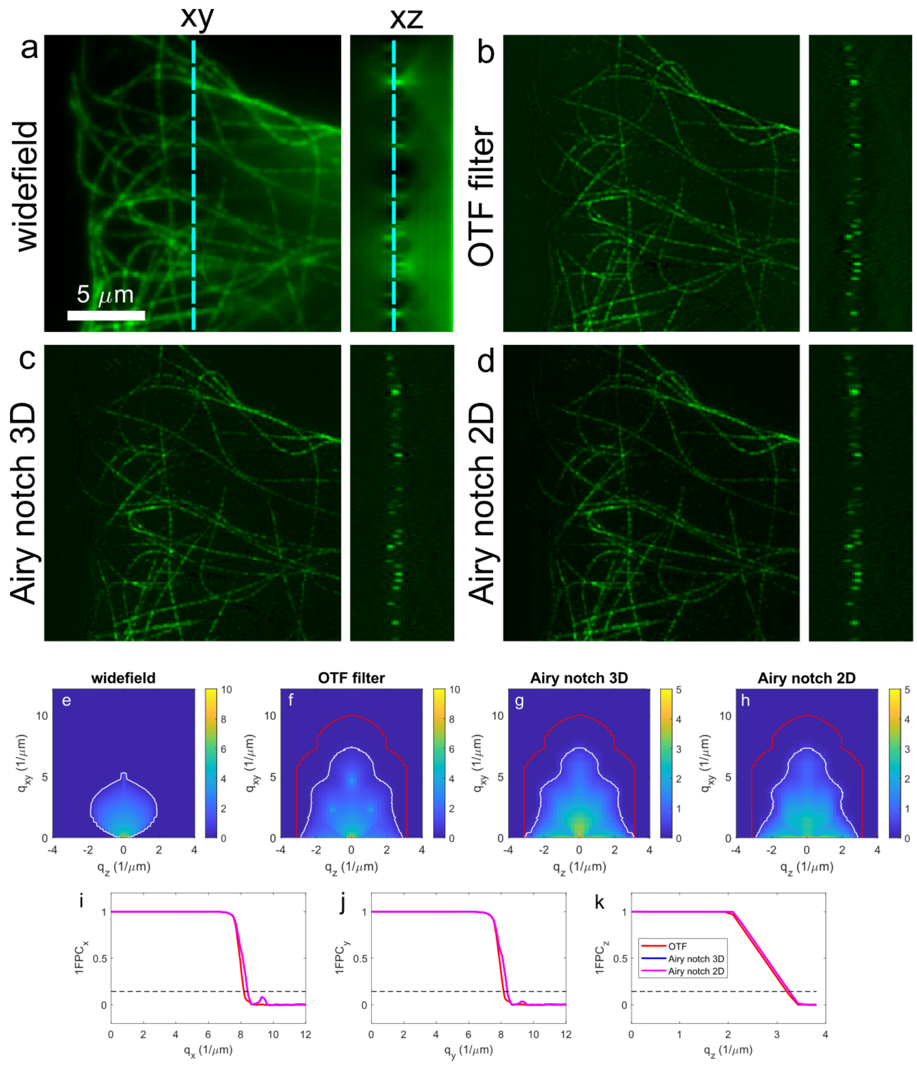

Fig. 8. Single colour 3D SIM reconstructions of tubulin. (a) Widefield reference. (b) Ideal OTF filtered SIM. (c) Airy notch filter with additional axial sinc filter. (d) Fully 2D Airy notch filter. All *xy* and *xz* slices have been contrast stretched to their minimum and maximum pixel value. (e-h) Measured ring averaged SSNR for widefield and the three SIM reconstructions. The colormaps are on a log-scale according to $\log_{10}(1 + SSNR)$. The red curves indicates the OTF support of SIM, the white curves are the $SSNR = 1$ contour lines, indicative of the Fourier space region with substantially non-zero SSNR. The colormap scale for the notch filtering cases is different from the widefield and OTF filtering cases to improve visibility. (i-k) Single image FPC curves in the *xyz* directions for the different filtering cases. The black dashed line indicates the 1/7 threshold.

Optics EXPRESS

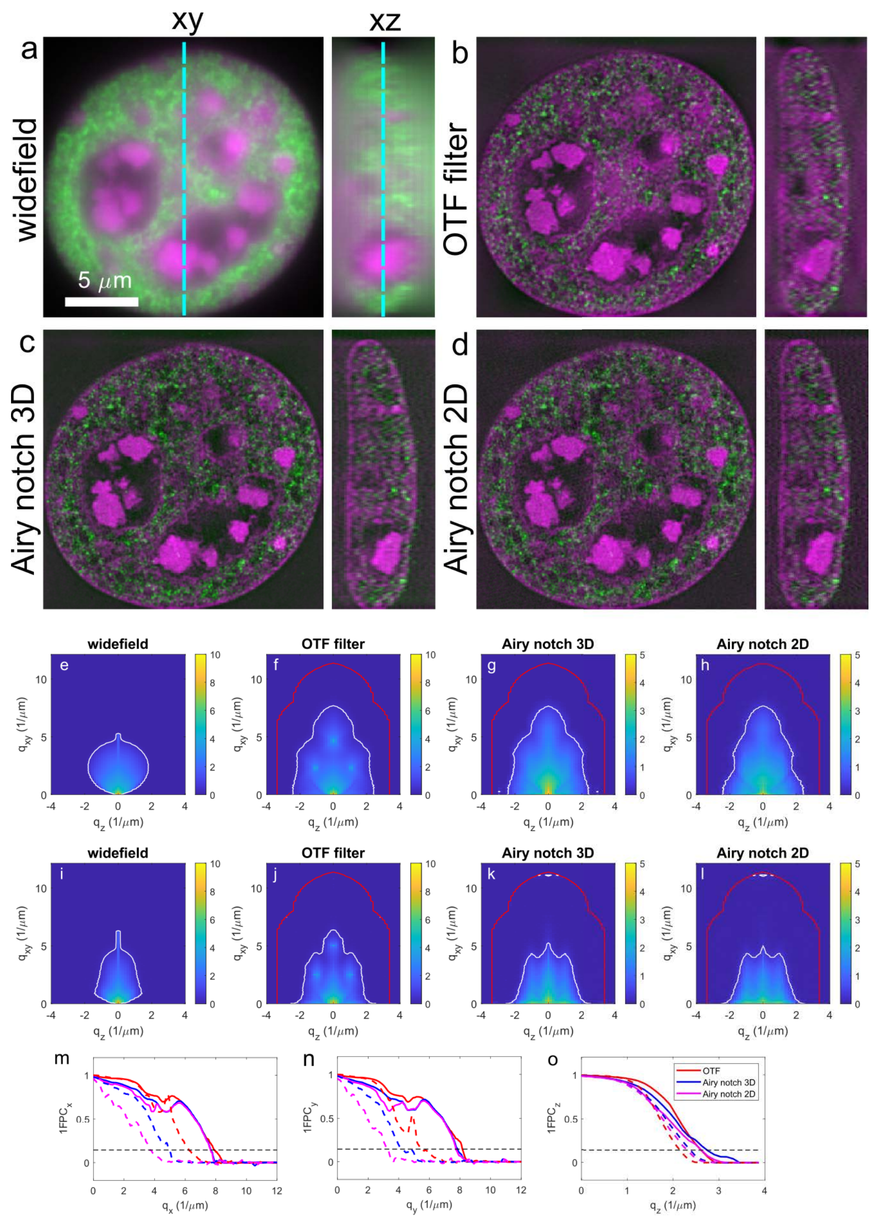

Fig. 9. Two colour 3D SIM reconstructions of a C127 cell (green channel H3K4me3, magenta channel DAPI). (a) Widefield reference. (b) Ideal OTF filtered SIM. (c) Airy notch filter with additional axial sinc filter. (d) Fully 2D Airy notch filter. All *xy* and *xz* slices have been contrast stretched to their minimum and maximum pixel value. (e-h) Measured ring averaged SSNR for widefield and the three SIM reconstructions for the H3K4me3 channel. (i-l) Measured ring averaged SSNR for widefield and the three SIM reconstructions for the DAPI channel. The colormaps are on a log-scale according to $\log_{10}(1 + SSNR)$. The red curves indicates the OTF support of SIM, the white curves are the $SSNR = 1$ contour lines, indicative of the Fourier space region with substantially non-zero SSNR. The colormap scale for the notch filtering cases is different from the widefield and OTF filtering cases to improve visibility. (m-o) Single image FPC curves in the *xyz* directions for the different filtering cases (full curves green channel, dashed curves magenta channel). The black dashed line indicates the 1/7 threshold.

notch 2D). For the magenta (DAPI) channel we do see quite a bit worse image resolutions for the Airy notch filtering cases, in agreement with the poorer SSNR heatmaps ($1FPC_{x,y,z}$ = 160, 181, 458 nm for OTF; $1FPC_{x,y,z}$ = 201, 236, 414 nm for Airy notch 3D; $1FPC_{x,y,z}$ = 272, 307, 426 nm for Airy notch 2D).

6. Discussion and outlook

In summary, we demonstrated a systematic way to assess the quality of SIM reconstructions based on SSNR. We showed that under the assumption of well-separated Fourier orders, the least-squares reconstruction provides the theoretically best achievable SSNR at each spatial frequency in the framework of linear reconstructions. We then used the FDR SSNR as a quantitative benchmark of the performance of other linear reconstructions.

We found that SDR can achieve nearly as good a SSNR as FDR with a relatively small convolution kernel. We introduced two families of the convolution kernels with a non-negative Fourier transform: OTF-like kernels for isotropic SSNR improvement and separable triangular kernels that have better behavior in terms of theoretical computational complexity.

We analyzed a common case where the real OTF is aberrated and unknown, and hence the conventional Fourier reconstruction uses a sub-optimal kernel that is equal to the ideal OTF. We showed that while aberrations themselves lead to a significant SSNR reduction, the error due to the mismatch between the physical and the reconstruction transfer functions is negligible. Also in this context, real-space reconstructions with a correctly-chosen finite kernel demonstrate nearly-ideal SSNR performance independent of the strength of the aberrations present in the physical OTF.

Finally, we proposed an alternative way to perform 3D SIM reconstructions, incorporating notch filtering and amplification of 1st and 2nd image Fourier orders. In this way, each slice of the 3D image is processed independently, and only the final contrast restoring Wiener filtering step remains to be done in 3D. We demonstrated that the optical sectioning capabilities of such a reconstruction are comparable with those of the least-squares Fourier domain reconstructions.

In this work, we have focused on the theoretical side of spatial domain reconstructions, and their actual computational performance on large 2D and 3D datasets is yet to be tested. In theory, the computational complexity of the reconstructions with finite kernels is trivial. Only $K \times K$ and $2K$ operations per pixel are required for the cases of unseparable and separable 2D kernels of size $K \times K$, respectively, that is around 20-100 operations per pixel in practical cases. However, modern FFT algorithms [43] are extremely optimized, while the hardware on the graphic cards is optimized for 2D operations. For these reasons, we expect to see a more prominent performance improvement in the case of 3D reconstructions.

Another fundamental limitation of real-space SIM reconstructions is that experimental images typically require 2x upsampling to accommodate the higher resolution of the SIM reconstruction, which is best done in the Fourier domain by means of zero padding. Real-space interpolation with a small kernel will inevitably introduce additional errors. It remains to be elucidated how small such errors can be made in practice.

Finite kernels may have other applications beyond the acceleration of the reconstruction. Fourier domain reconstructions suffer from edge effects; thus, real-space reconstructions may be preferable to avoid stitching artifacts when it is not possible to process the whole FOV in the Fourier domain at once. Edge artifacts and associated artifacts are also probably the reason for a slightly better optical sectioning achieved in our finite kernels 3D reconstruction in spite of the fact that the conventional reconstruction yields overall higher SSNR.

Another advantage of the finite kernels is that they result in a notably better contrast in case the Wiener-filtering procedure is impaired. Overall, the usage of finite kernels may have advantages in advanced experimental techniques, such as LS-SIM [44], which face complications such as a large amount of data, non-uniform background and prominent and field dependent aberrations.

Optics EXPRESS

Funding. European Research Council (101055013).

Acknowledgments. The authors are thankful to Rainer Heintzmann for useful discussions about the applications of finite kernels and the numerical complexity of SIM reconstructions.

Disclosures. The authors declare no conflicts of interest.

Data availability. The software used for SSNR calculations is available in [45], and the software used for experimental SIM reconstructions at [46]. Experimental data for SIM reconstructions can be found at [47].

Supplemental document. See Supplement 1 for supporting content.

References

1. R. Heintzmann and C. Cremer, "Laterally modulated excitation microscopy: Improvement of resolution by using a diffraction grating," Proc. SPIE **3568**, 185–196 (1999).
2. M. G. L. Gustafsson, "Surpassing the lateral resolution limit by a factor of two using structured illumination microscopy," J. Microsc. **198**(2), 82–87 (2000).
3. M. G. L. Gustafsson, L. Shao, P. M. Carlton, *et al.*, "Three-dimensional resolution doubling in wide-field fluorescence microscopy by structured illumination," Biophys. J. **94**(12), 4957–4970 (2008).
4. S. J. Wright and D. J. Wright, "Introduction to confocal microscopy," in *Methods in Cell Biology*, vol. 70 (Elsevier Science, 2002), pp. 1–85.
5. C. B. Müller and J. Enderlein, "Image scanning microscopy," Phys. Rev. Lett. **104**(19), 198101 (2010).
6. C. J. R. Sheppard, S. B. Mehta, and R. Heintzmann, "Superresolution by image scanning microscopy using pixel reassignment," Opt. Lett. **38**(15), 2889–2892 (2013).
7. G. M. R. D. Luca, R. M. P. Breedijk, R. A. J. Brandt, *et al.*, "Re-scan confocal microscopy: scanning twice for better resolution," Biomed. Opt. Express **4**(11), 2644–2656 (2013).
8. S. W. Hell and J. Wichmann, "Breaking the diffraction resolution limit by stimulated emission: stimulated-emission-depletion fluorescence microscopy," Opt. Lett. **19**(11), 780–782 (1994).
9. H. Blom and J. Widengren, "Stimulated emission depletion microscopy," Chem. Rev. **117**(11), 7377–7427 (2017).
10. C. J. R. Sheppard, "Super-resolution in confocal imaging," Optik **80**, 53–54 (1988).
11. S.-T. Hung, D. Kalisvaart, and C. S. Smith, "Image scanning microscopy: a vectorial physical optics analysis," Opt. Express **32**(2), 1524–1538 (2024).
12. S. Lim, S. Kang, J. H. Hong, *et al.*, "Dual deconvolution in multiphoton structured illumination microscopy for deep-tissue super-resolution imaging," Nat. Commun. **17**(1), 2123 (2026).
13. M. Schropp and R. Uhl, "Two-dimensional structured illumination microscopy," J. Microsc. **256**(1), 23–36 (2014).
14. V. Brudanin, B. Rieger, and S. Stallinga, "Comparison of 3D structured illumination microscopy configurations in terms of spectral signal to noise ratio," Opt. Express **33**(5), 11832–11852 (2025).
15. E. A. Ingerman, R. A. London, R. Heintzmann, *et al.*, "Signal, noise and resolution in linear and nonlinear structured-illumination microscopy," J. Microsc. **273**(1), 3–25 (2018).
16. C. S. Smith, J. A. Slotman, L. Schermelleh, *et al.*, "Structured illumination microscopy with noise-controlled image reconstructions," Nat. Methods **18**(7), 821–828 (2021).
17. S. Stallinga, N. Radmacher, A. Delon, *et al.*, "Optimal transfer functions for bandwidth-limited imaging," Phys. Rev. Res. **4**(2), 023003 (2022).
18. C. H. Righolt, J. A. Slotman, I. T. Young, *et al.*, "Image filtering in structured illumination microscopy using the Lukosz bound," Opt. Express **21**(21), 24431–24451 (2013).
19. I. Droste, E. Schuitema, S. A. Khan, *et al.*, "Calibration-free estimation of field-dependent aberrations for single-molecule localization microscopy across large fields of view," Optica **12**(8), 1220–1232 (2025).
20. R. Li, X. Zhou, D. Wu, *et al.*, "Selective plane illumination microscopy with structured illumination based on spatial light modulators," in *Three-Dimensional and Multidimensional Microscopy: Image Acquisition and Processing XXI*, vol. 8949 (SPIE, 2014), p. 89491S.
21. K. Temma, R. Oketani, T. Kubo, *et al.*, "Selective-plane-activation structured illumination microscopy," Nat. Methods **21**(5), 889–896 (2024).
22. P. T. C. So, H. S. Kwon, and C. Y. Dong, "Resolution enhancement in standing-wave total internal reflection microscopy: a point-spread-function engineering approach," J. Opt. Soc. Am. A **18**(11), 2833–2845 (2001).
23. D. Dan, Z. Wang, X. Zhou, *et al.*, "Rapid image reconstruction of structured illumination microscopy directly in the spatial domain," IEEE Photonics J. **13**(1), 1–11 (2021).
24. Z. Wang, T. Zhao, H. Hao, *et al.*, "High-speed image reconstruction for optically sectioned, super-resolution structured illumination microscopy," Adv. Photonics **4**(02), 026003 (2022).
25. T. Zhao, Z. Wang, Y. Cai, *et al.*, "Fast single-layer reconstruction for three-dimensional structured illumination microscopy," Opt. Laser Technol. **167**, 107606 (2023).
26. T. Zhao, Z. Wang, M. Shu, *et al.*, "Instant square lattice structured illumination microscopy: an optimal strategy towards photon-saving and real-time super-resolution observation," arXiv (2024).
27. C. E. Shannon, "Communication in the presence of noise," Proc. IRE **37**(1), 10–21 (1949).
28. H. Pinkard, L. Kabuli, E. Markley, *et al.*, "Universal evaluation and design of imaging systems using information estimation," arXiv (2024).

29. Q. Chen, W. Guo, W. Lu, *et al.*, "Fast, three-dimensional, live-cell super-resolution imaging with multiplane structured illumination microscopy," Nat. Photonics **19**(6), 567–576 (2025).
30. Q. Liu, D. Zhou, J. Zhang, *et al.*, "DMD-based compact SIM system with hexagonal-lattice-structured illumination," Appl. Opt. **62**(20), 5409–5415 (2023).
31. S. Abrahamsson, J. Chen, B. Hajj, *et al.*, "Fast multicolor 3D imaging using aberration-corrected multifocus microscopy," Nat. Methods **10**(1), 60–63 (2013).
32. S. Abrahamsson, H. Blom, A. Agostinho, *et al.*, "Multifocus structured illumination microscopy for fast volumetric super-resolution imaging," Biomed. Opt. Express **8**(9), 4135–4140 (2017).
33. A. Descloux, M. Müller, V. Navikas, *et al.*, "High-speed multiplane structured illumination microscopy of living cells using an image-splitting prism," Nanophotonics **9**(1), 143–148 (2020).
34. J. Joseph, K. P. Faiz, M. Lahrberg, *et al.*, "Improving the space-bandwidth product of structured illumination microscopy using a transillumination configuration," J. Phys. D: Appl. Phys. **53**(4), 044006 (2020).
35. I. T. Young and L. J. van Vliet, "Recursive implementation of the Gaussian filter," Signal Processing **44**(2), 139–151 (1995).
36. K. Wicker, O. Mandula, G. Best, *et al.*, "Phase optimization for structured illumination microscopy," Opt. Express **21**(2), 2032–2049 (2013).
37. M. Müller, V. Mönkemöller, S. Hennig, *et al.*, "Open-source image reconstruction of super-resolution structured illumination microscopy data in imagej," Nat. Commun. **7**(1), 10980 (2016).
38. C. Ji, Y. Zhu, E. He, *et al.*, "Full field-of-view hexagonal lattice structured illumination microscopy based on the phase shift of electro–optic modulators," Opt. Express **32**(2), 1635–1649 (2024).
39. S. Stallinga and B. Rieger, "Accuracy of the Gaussian point spread function model in 2D localization microscopy," Opt. Express **18**(24), 24461–24476 (2010).
40. A. van der Schaaf and J. H. van Hateren, "Modelling the power spectra of natural images: Statistics and information," Vision Res. **36**(17), 2759–2770 (1996).
41. B. Rieger, I. Droste, F. Gerritsma, *et al.*, "Single image Fourier ring correlation," Opt. Express **32**(12), 21767–21782 (2024).
42. R. P. J. Nieuwenhuizen, K. A. Lidke, M. Bates, *et al.*, "Measuring image resolution in optical nanoscopy," Nat. Methods **10**(6), 557–562 (2013).
43. M. Frigo and S. G. Johnson, "FFTW: Fastest Fourier Transform in the West," https://www.fftw.org/.
44. D. Li, L. Shao, B.-C. Chen, *et al.*, "Extended-resolution structured illumination imaging of endocytic and cytoskeletal dynamics," Science **349**(6251), aab3500 (2015).
45. V. Brudanin, "https://github.com/valbrud/SIM," (2024). GitHub repository.
46. C. Smith, "https://github.com/qnano/simnoise," (2021). GitHub repository.
47. C. S. Smith, J. A. Slotman, L. Schermelleh, *et al.*, "Supplementary data that support the findings of "Information driven structured illumination microscopy using noise-controlled image reconstructions"," (2020).